Imaging permafrost active layer thickness under forest for climate model improvement

Franck Garestier, S. Guillaso, A.V. Kouraev, Bertrand Decharme, R.V. Desyatkin, A. Desyatkin, T. Chevalier

International Journal of Applied Earth Observation and Geoinformation 125 (2023) 103582

Contents lists available at ScienceDirect

International Journal of Applied Earth Observation and Geoinformation

journal homepage: www.elsevier.com/locate/jag

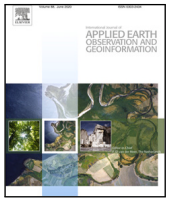

Imaging permafrost active layer thickness under forest for climate model improvement

F. Garestier [a,*], S. Guillaso [d], E.A. Zakharova [f,g], A.V. Kouraev [e], B. Decharme [h], R.V. Desyatkin [b], A. Desyatkin [b,c], T. Chevalier [a]

[a] Coastal and Continental Morphodynamics - UMR CNRS 6143 M2C- University of Normandy, Caen, France
[b] Institute for Biological Problems of Cryolithozone; Siberian Branch, Russian Academy of Science, Russia
[c] Melnikov Permafrost Institute, Siberian Branch, Russian Academy of Science, Russia
[d] Helmholtz Centre Potsdam GFZ German Research Centre for Geosciences Telegrafenberg, 14473 Potsdam, Germany
[e] Université de Toulouse, LEGOS (CNES/CNRS/IRD/UT3), Toulouse, France
[f] EOLA, Toulouse, France
[g] Water Problems Institute, RAS, Moscow, Russia
[h] Centre National de Recherches Météorologiques, Université de Toulouse, Météo-France, CNRS UMR 3589, Toulouse, France

ARTICLE INFO

Keywords:
InSAR
Permafrost
Active layer thickness

ABSTRACT

Permafrost is an important but poorly known carbon reservoir which is vulnerable to the high latitude accelerated warming. The projected thickening of its superficial seasonally thawed active layer and its induced spatial reorganization will hasten Carbon release in the atmosphere while impacting hydrology, geochemical transfers, vegetation repartition and ground stability. Active layer thickness (ALT) is only assessed by northern stations, therefore, its spatial distribution remains unknown and lacks for model evaluation, especially under the boreal forest. The all-weather spaceborne InSAR technique has shown only partial sensitivity to ALT through ground movements and remained restricted to non-forested areas. To overcome these limitations, we generalized the ground movement estimation under the omnipresent forest by exploiting the SAR polarimetric information, on the one side, and we isolated the thermodynamical component from the hydrological one during freezeback using a land surface model, on the other side, to extract ALT. Based on a one year TerraSAR-X time serie acquired over the region of Yakustk, we obtained a first high resolution ALT image which reveals unexpected short scale spatial heterogeneity, arranged along anisotrotopic patterns. Its poor comparison with the ALT simulated by the ISBA land surface model, currently used in climate modeling, highlights that climate models, and thus their simulations of greenhouse gas emissions, remain very uncertain over northern high latitudes in absence of regionalized ALT information under the boreal forest. This novel approach, operable using current and future sensors over wide areas, offers a new way forward to improve modeling as well as to optimally monitor global warming from the high latitudes.

1. Introduction

The Arctic currently warms at a rate that is twice as fast as the global average. The soil of permafrost regions is an important Carbon reservoir. Indeed, it holds almost two times the Carbon that is currently present in the atmosphere: last update attests of 1014 PgC content in the top 3 m of the 2300 continental PgC pool (Mishra et al., 2021). Hence, permafrost degradation contributes to global warming by releasing greenhouse gases (Schuur et al., 2015; Zimov, 2006), as carbon dioxide and methane, the global warming potential of the latter being around 30 times higher (Morel et al., 2019). The ALT, defined as the depth reached by the 0 °C isotherm in the soil during summer, represents one of the most robust measures to assess the impact of climate change on terrestrial permafrost. In addition, all the biogeochemical processes responsible for carbon pool degradation, and thus greenhouse gas emissions, are located into this ALT, which constitute one of the main Permafrost Essential Climate Variables (Biskaborn et al., 2019).

Besides greenhouse gases, thickening of ALT has important implications for hydrological processes, that also affect the albedo of the land surface in a positive feedback loop accelerating the thaw of ice-rich permafrost, sediment transport (Bonnaventure and Lamoureux, 2013) and soil geochemistry (Kokelj and Burn, 2005; Tashiro et al., 2020).

* Corresponding author.
E-mail address: franck.garestier@unicaen.fr (F. Garestier).

https://doi.org/10.1016/j.jag.2023.103582
Received 5 April 2023; Received in revised form 2 November 2023; Accepted 18 November 2023
Available online 5 December 2023

ALT has a close relationship with the vegetation cover as it is influenced by forest species (Fedorov et al., 2019) and, conversely, could cause shifts in ecosystem vegetation (Bonnaventure and Lamoureux, 2013). Finally, ALT disturbance may be the source of hazards such as floods, subsidence, generation of thermokarst ponds or mass movements (rock falls, debris flows, retrogressive thaw slumps and active layer detachment failures), and, consequently, may have many social and economic consequences in the populated areas (Bonnaventure and Lamoureux, 2013).

Nowadays, ALT is primarily assessed through *in-situ* techniques (probing and northern stations of Circumpolar Active Layer Monitoring Program), but the scarce network of monitoring sites makes it impossible to comprehensively document its statistical and spatial distribution over large periglacial regions (Fagan and Nelson, 2016). Therefore, accurate representation of ALT spatial variability, occurring at different scales, from some meters to hundreds of meters (Nelson et al., 1999), is a prerequisite for reducing existing uncertainty of ecosystem and climate models (Nelson et al., 1999; Beer et al., 2013; Fisher et al., 2018). Significant shortcomings in estimation of ALT distribution have stimulated interest in development of spaceborne approaches, especially using SAR technique thanks to its low dependency on weather conditions and to its global coverage. Due to changes of groundwater state during the freeze-thaw cycle, the thaw depth variation induces surface vertical deformation of small -millimeter to centimeter-scale (Shiklomanov et al., 2013). During the past decade, SAR Differential Interferometry (D-InSAR) (Biggs and Wright, 2020) derived surface deformation, from time series up to several years, has been shown to be partially only related to ALT over non-forested areas (Liu et al., 2010; Daout et al., 2017; Strozzi et al., 2018; Antonova et al., 2018; Bartsch et al., 2019; Abe et al., 2020), that has led to physical modeling for development of inversion algorithms (Liu et al., 2012; Schaefer et al., 2015). More recently, temporal fits of deformation derived from a slightly non-linear inversion approach (Berardino et al., 2002) exhibit seasonal cycles, that differ from one geomorphologic feature to another, and match the ground thawing and freezing periods (Rouyet et al., 2019, 2021). By the same token, strategies based on seasonal behavior of the deformation are proposed to detect ice rich top-layer permafrost in late summer (Zwieback and Meyer, 2021). However, subsurface hydrological circulations can act as an additional dynamic component of the ground deformation. To overcome the existing limitations of ALT inversion from D-InSAR, we exploited the polarimetric information to generalize the estimation of ground deformation below the forests, on the one hand, and we analyzed the whole freeze-thaw cycle using the ISBA (Interaction-Soil-Biosphere-Atmosphere) land surface model (Decharme et al., 2016, 2019) to isolate the thermodynamical component of the ground deformation (processes induced by the water state variations), on the other hand.

In Methodology section, we first expose the theoretical developments for estimating the ground deformation below the forest using InSAR time series. In Result section, the entire freeze-thaw cycle is scanned to identify the processes occurring in the ground. From this, ISBA land surface model is used to extract the ALT.

2. Methodology

2.1. InSAR acquisitions, pre-processing and test site description

The SAR acquisitions have been performed near Yakutsk, Russia, using TerraSAR-X sensor in stripmap mode during the whole 2013 year, with a high resolution (1.8 × 2.4 m) and a 11 day time revisit, at HH/HV dual-pol. The coregistration of the TSX images has become a challenge over regions affected by extreme weather conditions, because the scatterers can evolve importantly over small periods. As amplitude correlation approaches can be not robust enough, a method using only the orbits has been preferred. The TerraSAR-X images are delivered with a serie of tie-points serving as reference, from which we obtain the geolocation and the height. Using the radar equations and applying the corrections mentioned in Fritz et al. (2008), Breit et al. (2010), it is possible to derivate an accurate estimate of the offset between the two images. Then, a polynomial function is estimated from these points and the slave images are warped. To preserve polarimetric information, both polarimetric slave images are warped using this common function. The pre-processing used in this study is based on a modified version of the NSBAS pre-processing chain proposed in Doin et al. (2011) and the InSAR processing workflow is summarized in Supplementary Data Fig. 1.

Over permafrost regions, all the surfaces are likely to be affected by deformation. Therefore, the interferometric calibration has been performed using a fixed point (62°06'45N/130°01'53E): the deepest foundation building (geotechnical requirement preventing from shear failure of walls of large buildings) over the 57 × 17 km swath. The roof of the building is large enough to contain various pixels free of any layover. The scattering mechanism occurring over the roof is characterized by a high backscatter, constant in time. The important SNR and, associated low phase noise, ensures a reliable phase calibration: it will be shown in Section 3.1 that the interferograms formed during winter show a similar zero mean interferometric phase.

The following subsections will describe how to proceed for ground movement estimation under forest. It includes ground interferometric phase estimation, which involves polarimetric coherence optimization, and removal of the ground topography (in red in Supplementary Data Fig. 1).

The region of Yakutsk, one of the world coldest cities, has been chosen since it is representative of the continuous permafrost environment of central Siberia (Fedorov et al., 2019), where the annual temperature span reaches world record highs, of the order of 100 °C. Fig. 5a locates the swath of the SAR images over the first eastern terraces of the Lena River, which is entirely covered by boreal forest (forests cover large part of the permafrost environment: 12 million square kilometers). It is mainly composed of larches, of pines in lesser degree and of few birches on the burns and clearings, which surrounds alaces (glade often including lake and pingo) and thermokarst lakes. Several ground measurement compaigns have concerned the forest height, the ground topography along transects, the ALT and the soil/vegetation characterization, during the past ten years.

2.2. Estimation of the ground deformation below the forest

SAR polarimetric interferometry (Cloude and Papathanassiou, 1998) exploits the polarimetric diversity of the interferometric information to separate ground and forest contributions. The interferometric coherence associated with a polarization $\boldsymbol{\omega}$ is expressed as,

$$\gamma(\boldsymbol{\omega}) = \frac{\boldsymbol{\omega}^{\dagger}\boldsymbol{\Omega}_{12}\boldsymbol{\omega}}{\sqrt{\boldsymbol{\omega}^{\dagger}\boldsymbol{T}_{11}\boldsymbol{\omega}\boldsymbol{\omega}^{\dagger}\boldsymbol{T}_{22}\boldsymbol{\omega}}} \tag{1}$$

$\boldsymbol{T}_{ii}$ are the polarimetric coherency matrixes and $\boldsymbol{\Omega}_{12}$ contains the polarimetric interferometric information. By defining $\boldsymbol{T} = \frac{\boldsymbol{T}_{11}+\boldsymbol{T}_{22}}{2}$, it can be contracted as (Flynn et al., 2002),

$$\gamma(\boldsymbol{\omega}) = \boldsymbol{\omega}^{\dagger}\boldsymbol{T}^{-\frac{1}{2}}\boldsymbol{\Omega}_{12}\boldsymbol{T}^{-\frac{1}{2}}\boldsymbol{\omega} \tag{2}$$

The contraction will not affect the interferometric phase but can lower the coherence if the polarimetric coherency matrixes $\boldsymbol{T}_{ii}$ show important difference. In our successive acquisition approach, the linear values of both HH and HV backscatter never differ of more than 30% among the interferometric pairs, then the regions of coherence drawn by Eqs. (1) and (2) remain stackable in the complex plane.

Forest is represented by two layers, corresponding to ground and canopy (Cloude and Papathanassiou, 2003; Cloude, 2009; Lee and Pottier, 2017). Interferometric coherence associated with a polarimetric channel $\boldsymbol{\omega}$ can be formulated as,

$$\gamma(\boldsymbol{\omega}) = \frac{m(\boldsymbol{\omega})|\gamma_g| + |\gamma_{tv}|\gamma_v(\boldsymbol{\omega})}{1 + m(\boldsymbol{\omega})} e^{j\phi_0}$$

$$0 \leq m(\boldsymbol{\omega}) < +\infty$$

where γ_g and γ_v are the ground and volume interferometric coherences, respectively, ϕ_0 denotes the ground interferometric phase, m is the ground to volume power ratio and $|\gamma_{tv}|$ is the volume temporal decorrelation term.

The balance between ground and canopy components varies from a polarimetric channel to another. At high frequency, interaction with the canopy mostly occurs in its upper part, therefore, the sensitivity of the interferometric signal to the forest structure is low (De Zan et al., 2013; Garestier et al., 2008; Treuhaft et al., 2015). As the structure seen at different polarizations remains the same, contrary to low frequency (Hosseini and Garestier, 2021), the associated interferometric coherences are spread over a line in the complex plane and their position on the line are determined by their ground to volume power ratio. The line is bounded by ground and canopy interferometric coherences, independently of the complexity of the latter. Eq. (3) is the generalized version of Garestier and Toan (2010a,b) to any forest structure, represented by a sum of truncated Gaussians characterized by relative elevations δ_i and standard deviations χ_i, weighted by coefficients c_i (Fig. 1a).

$$\gamma_v = \frac{\int_0^{h_v} e^{jk_z z} \sum_k c_k e^{-\frac{(z-\delta_k)^2}{2\chi_k^2}} dz}{\int_0^{h_v} \sum_k c_k e^{-\frac{(z-\delta_k)^2}{2\chi_k^2}} dz}$$
$$= \left(\prod_i e^{-\frac{\chi_i^2 k_z^2}{2}}\right) \times \left(\sum_k c_k \chi_k e^{j\delta_k k_z} \prod_{l\neq k} e^{\frac{\chi_l^2 k_z^2}{2}} \frac{erf\left(\frac{1}{\sqrt{2}}\left(j\chi_k k_z + \frac{\delta_k}{\chi_k}\right)\right) - erf\left(\frac{1}{\sqrt{2}}\left(j\chi_k k_z + \frac{\delta_k - h_v}{\chi_k}\right)\right)}{erf\left(\frac{h_v-\delta_k}{\sqrt{2}\chi_k}\right) + erf\left(\frac{\delta_k}{\sqrt{2}\chi_k}\right)}\right) \tag{3}$$

k_z is the vertical wavenumber, which related to the height of ambiguity by $k_z = 2\pi/Ha$.

For each forest structure, the intersection of the region of coherence regression line with the trigonometric circle localizes the ground interferometric coherence (Fig. 1b). The field of values $\mathcal{W}$ of $\boldsymbol{\Gamma} = \boldsymbol{T}^{-\frac{1}{2}} \boldsymbol{\Omega}_{12} \boldsymbol{T}^{-\frac{1}{2}}$ draws an ellipse of which foci, corresponding to its eigenvalues λ_i, are used to linearly extrapolate the ground interferometric phase, after SNR compensation (see "SNR compensation" below).

During its phenological cycle, change of the boreal forest structure will induce migration of the volume interferometric coherence γ_v in the complex plane and rotation of the line around the invariant ground interferometric coherence (Grey line in Fig. 1b). Also, variations of the weather conditions (temperature, precipitations, etc.) can affect the ground to volume power ratio, inducing a translation of the region of coherence along the line (red dashed arrow). Finally, temporal decorrelation of the vegetation layer occurring during the sensor revisit time induces radial translation of the volume interferometric coherence toward the center of the trigonometric circle, and a linear translation of the ellipse foci in the same direction (blue dashed arrows), without impacting the ground interferometric coherence estimation.

The ground deformation simply adds a ϕ_d phase rotation to the two layer representation in the complex plane (Fig. 2a). Usually, the ground phase is estimated through linear extrapolation of the foci but high frequency is known to be highly subject to temporal decorrelation (Sica et al., 2021) and the canopy component appears fully decorrelated after the 11 day revisit. The volume interferometric coherence migrates then toward the origin of the complex plane and the ellipse region of coherence aligns with its radial dimension (its angle corresponds to the interferometric phase of the ground). Indeed, we verified that the interferometric phases of the foci displayed similar patterns in the whole time serie and differed only by their SNR. Then, in this special case, the phase of the optimal interferometric coherence becomes equivalent to the linear extrapolation (Fig. 2a),

$$\lim_{|\gamma_{tv}|\to 0} (Arg\{\gamma_{opt}\}) = \phi_0 + \phi_d \tag{4}$$

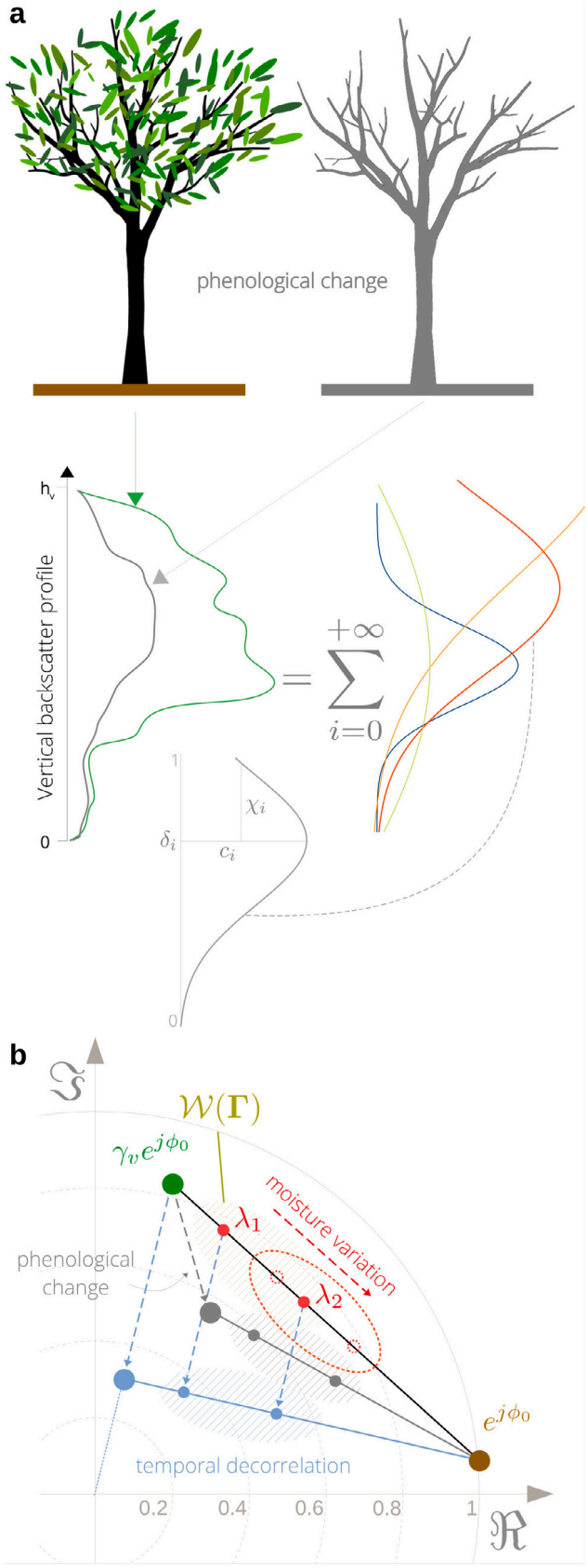

Fig. 1. Vegetation influence on ground phase estimation. **a,** Description of forest structure complexity using infinite sum of truncated Gaussians. **b,** Representation in the complex plane of the effects of forest structure complexity, phenological change, weather conditions and temporal decorrelation on ground phase estimation. (For interpretation of the references to color in this figure legend, the reader is referred to the web version of this article.)

Note that to estimate ground deformation, the topographic compensation would theoretically require the DEM of the ground below the forest but it is not available. The strategy we employed consists in estimating the ground topographic phase from the data itself (see "Toptographic compensation of the ground" below). In the natural canopies, characterized by relatively low densities, gaps enable the reception of the ground contribution, potentially even in HV channel. Contrasted ground to canopy power ratios in the polarimetric channels radially extend the region of coherence and then, the optimization brings the advantage of improving the accuracy of the ground phase estimate compared to the linear extrapolation (Fig. 2b). In fact, the lower the foci coherence is, the higher its associated phase standard deviation, imprecisions would then be propagated through the linear extrapolation whereas optimization brings stability. Example of deformation maps estimated after Goldstein filtering (Goldstein and Werner, 1998) are provided in Fig. 2c over two contrasted areas. The first contains the frozen Lena River with its alluvial plain and boreal forest surrounding alaces and lakes (appearing highly colored because of ice fracturation). The second includes bare surfaces and forest, also surrounding alaces and lakes. HH shows, of course, higher coherence than HV, except for Lena River. The high phase noise of HV is responsible for the low performance of the linear extrapolation for accurate ground phase estimation. Polarimetric coherence optimization improves the deformation map quality, through minimization of the phase standard deviation, and extending the coherent spatial areas, as expected. We verify that it does not introduce any bias compared to the usual linear extrapolation approach, as attested by the zero centered histogram of phase difference between the linear extrapolation and optimization shown in Fig. 2d.

2.3. Polarimetric optimization closed form

The ellipse drawn in the complex plane by the field of values $\mathcal{W}$ of $\boldsymbol{\Gamma} = \boldsymbol{T}^{-\frac{1}{2}}\boldsymbol{\Omega}_{12}\boldsymbol{T}^{-\frac{1}{2}}$ has foci corresponding to its eigenvalues λ_i and semi-axes a and b, defined as follows,

$$a = \frac{1}{2}\sqrt{Tr(\boldsymbol{\Gamma}^{\dagger}\boldsymbol{\Gamma}) - 2\Re\{\lambda_2\lambda_1^*\}} \tag{5}$$

$$b = \frac{1}{2}\sqrt{Tr(\boldsymbol{\Gamma}^{\dagger}\boldsymbol{\Gamma}) - \|\lambda_1\|^2 - \|\lambda_2\|^2} \tag{6}$$

Angular position of interferometric coherence depends on its phase (topography, deformation) and its radial position is only related to coherence.

To obtain a closed-form solution of the coherence optimization problem, it is necessary to translate the referential to the center of the ellipse and to rotate it along one of its axes (Grey (x, y) space in Fig. 3). In this way, the number of unknowns becomes minimum for the ellipse description, allowing a appropriate Lagrangian problem formulation. It remains then to maximize the distance between the ellipse and the center of the trigonometric circle. The solution point will be the optimal coherence after back-translation/rotation to the complex plane referential.

The coordinates of the center of the ellipse in the complex plane is $\frac{1}{2}Tr(\boldsymbol{\Gamma})$. Its orientation is given by,

$$\alpha = \pi - tan^{-1}\left(\frac{\Im\{\lambda_1 - \lambda_2\}}{\Re\{\lambda_1 - \lambda_2\}}\right) \tag{7}$$

The ellipse center is translated of $[-\frac{1}{2}\Re\{Tr(\boldsymbol{\Gamma})\}, -\frac{1}{2}\Im\{Tr(\boldsymbol{\Gamma})\}]$ from the complex plane origin.

The translation-rotation matrix is defined as,

$$\mathbf{M} = \begin{bmatrix} \cos\alpha & -\sin\alpha & \frac{1}{2}(\Im\{Tr(\boldsymbol{\Gamma})\}\sin\alpha - \Re\{Tr(\boldsymbol{\Gamma})\}\cos\alpha) \\ \sin\alpha & \cos\alpha & -\frac{1}{2}(\Re\{Tr(\boldsymbol{\Gamma})\}\cos\alpha + \Im\{Tr(\boldsymbol{\Gamma})\}\sin\alpha) \\ 0 & 0 & 1 \end{bmatrix} \tag{8}$$

Considering the referential of the ellipse, aligned along the x axis, the coordinates of the center of the trigonometric circle is given by,

$$\begin{bmatrix} x_0 \\ y_0 \\ 1 \end{bmatrix} = \mathbf{M}\begin{bmatrix} 0 \\ 0 \\ 1franc \end{bmatrix} \tag{9}$$

The new coordinates of the center of the trigonometric circle become $\{\Re\{Tr(\boldsymbol{\Gamma})e^{j\alpha}\}, \Re\{Tr(\boldsymbol{\Gamma})e^{-j\alpha}\}\}$.

Distance optimization on a centered aligned ellipse from a point $C(x_0, y_0)$ is expressed under a Lagrangian formulation as,

$$\mathcal{L} = f(x, y) - \mu g(x, y) \quad \text{then} \tag{10}$$

$$\nabla f(x, y) = \mu \nabla g(x, y) \quad \text{with} \tag{11}$$

$$f(x, y) = (x - x_0)^2 + (y - y_0)^2 \tag{12}$$

$$g(x, y) = x^2/a^2 + y^2/b^2 - 1 \tag{13}$$

The optimum is found with,

$$\begin{aligned} \partial\mathcal{L}/\partial x = 0 \rightarrow x = \frac{x_0 a^2}{\mu + a^2} \\ \partial\mathcal{L}/\partial y = 0 \rightarrow y = \frac{y_0 b^2}{\mu + b^2} \end{aligned} \tag{14}$$

Injecting Eq. (14) in the ellipse equation leads to,

$$\frac{x_0^2 a^2}{(\mu + a^2)^2} + \frac{y_0^2 b^2}{(\mu + b^2)^2} - 1 = 0 \tag{15}$$

From this, a polynomial is formulated as,

$$\begin{aligned} -\mu^4 - (2b^2 + 2a^2)\mu^3 + (x_0^2 a^2 + y_0^2 b^2 - a^4 - b^4 \\ -4a^2 b^2)\mu^2 + (2a^2 b^2(x_0^2 + y_0^2) - 2(a^2 b^4 + a^4 b^2)) \\ \mu + x_0^2 a^2 b^4 + y_0^2 a^4 b^2 - a^4 b^4 = 0 \end{aligned} \tag{16}$$

The polynomial roots μ_i will allow to estimate the coordinates of the point maximizing the distance with the origin of the complex plane $C(x_0, y_0)$ in the (x, y) space. Four roots are obtained: a real one corresponding to coherence maximization, another real one associated with coherence minimization and two others that are complex conjugate. By defining a two element vector containing the two real roots as $\boldsymbol{\mu_v} = \{\mu_i \in \mathbb{R}\}$, the solution root $\hat{\mu}$ is obtained by the following norm maximization: $\| \frac{x_0}{\mu_v/a^2+1} + j\frac{y_0}{\mu_v/b^2+1} \|_{\infty}$.

Then, the farest point of the ellipse from the center of the trigonometric circle is placed in the referential of the complex plane using the following inverse transformation matrix,

$$\mathbf{M}^{-1} = \begin{bmatrix} \cos\alpha & \sin\alpha & \frac{1}{2}\Re\{Tr(\boldsymbol{\Gamma})\} \\ -\sin\alpha & \cos\alpha & \frac{1}{2}\Im\{Tr(\boldsymbol{\Gamma})\} \\ 0 & 0 & 1 \end{bmatrix} \tag{17}$$

Finally, the optimized interferometric coherence γ_{opt} is obtained using,

$$\begin{bmatrix} \Re\{\gamma_{opt}\} \\ \Im\{\gamma_{opt}\} \\ 1 \end{bmatrix} = \mathbf{M}^{-1}\begin{bmatrix} \frac{x_0}{\hat{\mu}/a^2+1} \\ \frac{y_0}{\hat{\mu}/b^2+1} \\ 1 \end{bmatrix} \tag{18}$$

2.4. SNR compensation

Considering a stationary $NE\sigma_0$, the SNR corresponding to each foci (associated with each eigenvector $\boldsymbol{\omega}_{opt_i}$) is,

$$SNR(\boldsymbol{\omega}_{opt_i}) = \frac{\boldsymbol{\omega}_{opt_i}^{\dagger}\boldsymbol{T}\boldsymbol{\omega}_{opt_i}}{\boldsymbol{\omega}_{opt_i}^{\dagger}\boldsymbol{T_n}\boldsymbol{\omega}_{opt_i}} \tag{19}$$

with the coherency matrix of the noise,

$$\boldsymbol{T_n} = \begin{bmatrix} <|n_{HH}|^2> & 0 \\ 0 & <|n_{HV}|^2> \end{bmatrix} \tag{20}$$

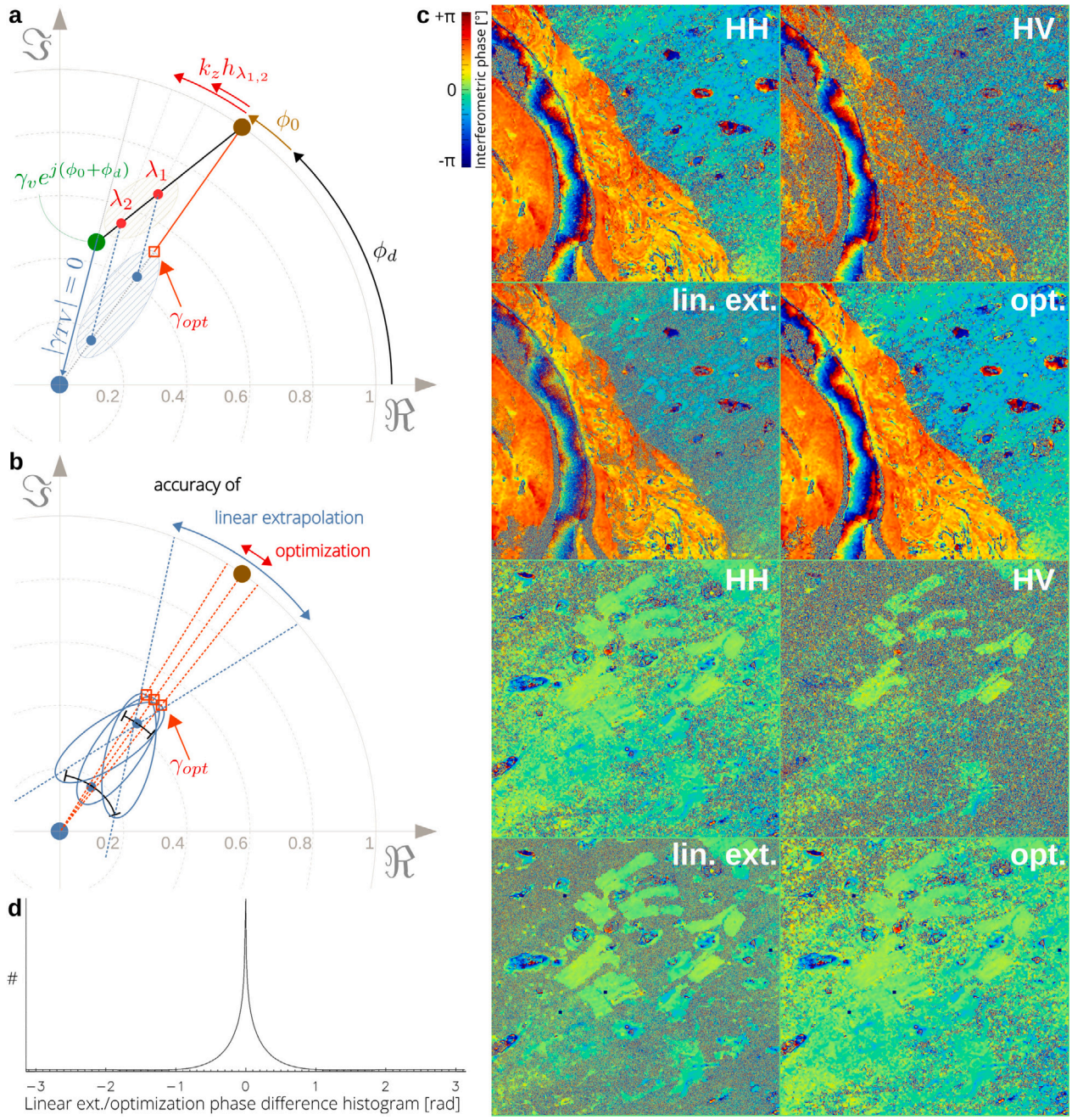

Fig. 2. Coherence optimization for ground deformation estimation. a, Representation of the region of coherence associated with a forest over ground medium in the complex plane in context of deformation. Effect of a full temporal decorrelation of the canopy in blue and localization of the optimal interferometric coherence γ_{opt}. **b,** Illustration of accuracies of both linear extrapolation and optimization derived ground phase estimates. **c,** Example of maps of deformation for HH, HV, linear extrapolation and optimization derived deformation, over two different areas. **d,** Linear extrapolation and optimization phase difference histogram. (For interpretation of the references to color in this figure legend, the reader is referred to the web version of this article.)

The amplitude ratio of the interferometric pair associated with each foci is defined as,

$$\alpha = \sqrt{\frac{\boldsymbol{\omega}_{opt_i}^{\dagger} \boldsymbol{T}_{11} \boldsymbol{\omega}_{opt_i}}{\boldsymbol{\omega}_{opt_i}^{\dagger} \boldsymbol{T}_{22} \boldsymbol{\omega}_{opt_i}}} \tag{21}$$

Then, from the SNR of the first image SNR_1, we infer,

$$\gamma_{SNR} = ((1 + \alpha^{-1} SNR_1^{-1})^2 + (1 - \alpha^{-1})^2 SNR_1^{-1})^{-1/2} \tag{22}$$

The SNR impacts the coherence and then the phase standard deviation. In the complex plane, the SNR compensation will correct for radial position only, which is essential for unbiased linear extrapolation of the ground phase and for the polarimetric coherence optimization. Practically, SNR correction is applied to each ellipse foci, which are translated in the radial dimension of the complex plane.

An illustration of the validation of the approach using GPS can be seen in Supplementary Data Fig. 2.

2.5. Topographic compensation of the underlying ground

Because of the impossibility to maintain a GPS station during an entire year in the non populated parts of the Yakutsk's region, the interferometric phase of the whole InSAR stack has been calibrated using a wide building having deep foundation structures, as mentioned

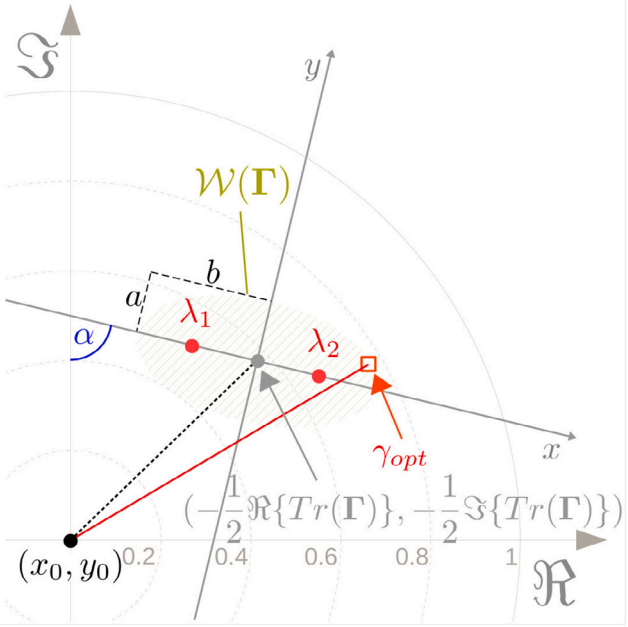

Fig. 3. Polarimetric coherence optimization. Change of referential in the complex plane.

in Section 2.1. The height of ambiguity of the used InSAR pairs always exceeds 80 m and is mainly in the 200–300 m range. The topographic contribution in the interferometric phase is low but may have some influence on the smallest deformations and/or for small perpendicular baselines. ArcticDEM is available at high latitude and has been re-sampled according to the master image of our interferometric stack. However, it has been acquired by optical sensors in this region and corresponds to the top of the canopy. Hence, to unbiasely correct for ground topographic phase, we employed a simple approach relying of the well known linear relation between vertical wavenumber and topographic component of the interferometric phase (Bombrun et al., 2009). We define $\boldsymbol{W}_{\phi}$, which contains the unwrapped optimal phase of the InSAR stack for a given pixel, corresponding to the ground below the forest, and $\boldsymbol{k}_z$, which is the vector containing the associated local vertical wavenumbers. As the vertical wavenumber is randomly distributed in time, the deformation component acts as an additive noise in the $\boldsymbol{W}_{\phi}$-$\boldsymbol{k}_z$ space. Fig. 4a illustrates three possible cases: null deformation (grey), zero mean deformation (green) and non-zero mean deformation (blue). To estimate the linear relation between the topographic component $\boldsymbol{W}_{\phi}$ and $\boldsymbol{k}_z$, and to filter the deformation one, we form the following covariance matrix,

$$\boldsymbol{C} = \begin{bmatrix} < |\boldsymbol{W}_{\phi} - < \boldsymbol{W}_{\phi} > |^2 > & < (\boldsymbol{k}_z - < \boldsymbol{k}_z >)(\boldsymbol{W}_{\phi} - < \boldsymbol{W}_{\phi} >) > \\ < (\boldsymbol{W}_{\phi} - < \boldsymbol{W}_{\phi} >)(\boldsymbol{k}_z - < \boldsymbol{k}_z >) > & < |\boldsymbol{k}_z - < \boldsymbol{k}_z > |^2 > \end{bmatrix} \tag{23}$$

The slope of the first eigenvector $\boldsymbol{v}_{opt_1}$ of the $\boldsymbol{C}$ covariance matrix is equal to the height, as shown in Fig. 4a. In this way, the height is retrieved in both cases of null or non-null mean deformations.

The relevance of this approach relies on the fact that we use interferograms associated with the deep winter period. The corresponding low temporal decorrelation added to the polarimetric coherence optimization ensure high enough coherence over the whole image to perform secure phase unwrapping: during this period, the interferograms are all characterized by continuous high enough coherence, i.e. without any decorrelated regions interrupting the phase continuity. Also, this approach is all the more robust as the ground phase estimation remains independent of the variations of phenology, of environmental

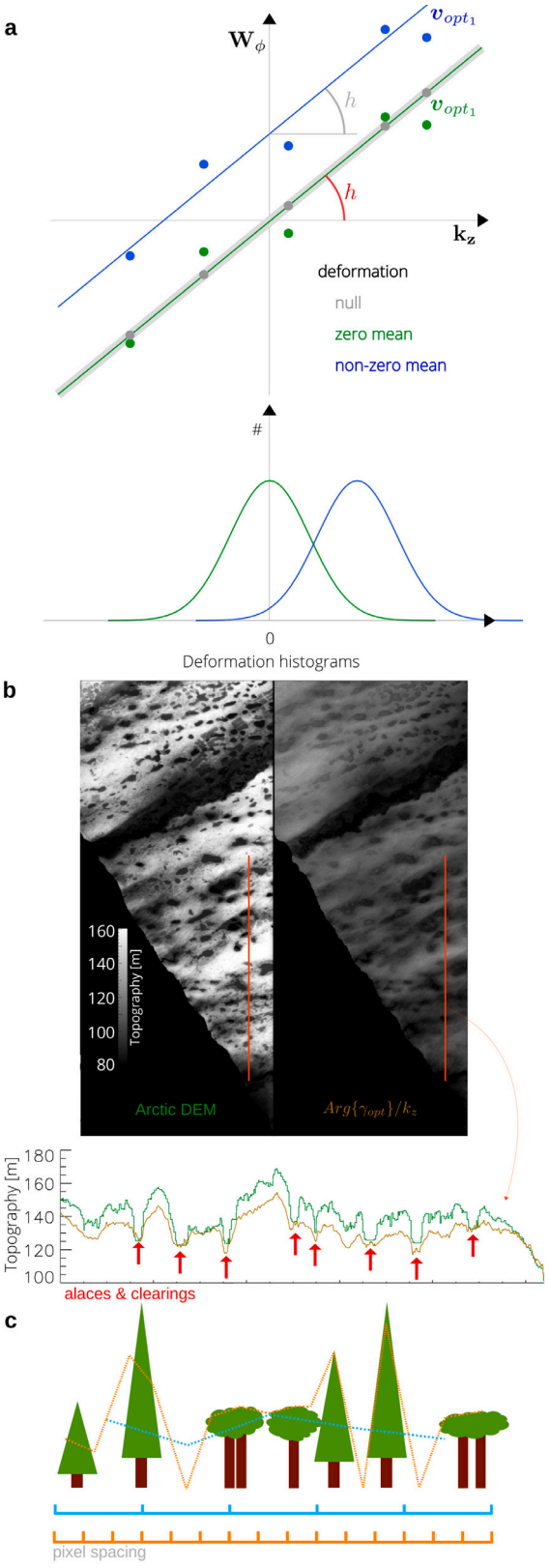

Fig. 4. Ground topographic phase removal. a, Unwrapped phase of the InSAR stack associated with a given pixel as a function of the corresponding local vertical wavenumber. Two case are considered: null or non-null mean deformation. **b,** Re-sampled ArcticDEM and optimal phase derived ground topography (top). Topographic profile associated with ground and top of canopy (bottom). **c**, Illustration of optical photogrammetric DEM of a forest at different pixel spacings.

conditions and of temporal decorrelation (see Section 2.2). Note finally that such approach is also helped by the high spatial resolution of TerraSAR-X avoiding any aliasing (2π jumps occur at least within several pixels).

The difference between ArcticDEM and the estimated ground DEM is proportional to the vegetation height but they become similar over alaces and clearings as shown in the topographic profile of Fig. 4b. In fact, This difference is equal to the vegetation height "seen" by photogrammetry at the SAR image resolution. As illustrated by Fig. 4c, increasing the pixel spacing extents averaging and can induce lowering of some individual tree height, depending on the canopy shape and tree density. Note that the ground height accuracy is estimated under 4 m, placing the topographic residual error inferior to the phase noise of the interferograms. The difference between ArcticDEM and the estimated ground DEM is then consistent with our various tree height measurements.

2.6. Atmospheric phase mitigation

The potential contribution from the stratified atmosphere, over this low topography region, was mitigated by the topographic compensation approach, based on linear relationship between residual phase and topography (Cavalié et al., 2007). However, as permafrost regions are affected by potential strong non-linear deformations, we chose to avoid performing SBAS-type inversions. In fact, the required polarimetric coherence optimization for ground deformation estimation makes possible to follow the deformation in time using individual interferograms. But for securing the interpretations, the deformation maps which have been selected have shown similar patterns at least over another independent interferogram, as in Chen et al. (2020).

2.7. ISBA land surface model

Interaction-Soil-Biosphere-Atmosphere (ISBA) land surface model (Decharme et al., 2016, 2019) which is operated in all climate models (Voldoire et al., 2019; Séférian et al., 2019) at Météo-France will be employed to extract ALT from InSAR estimated deformation. ISBA calculates time variations of energy and water budgets in 14 soil layers accounting for vegetation processes. The soil water content varies with surface infiltration, soil evaporation, plant transpiration and deep drainage. The soil ice content tendency (partial time derivative) is solved explicitly in each layer of the soil and accounts for ice sublimation and vegetation insulation effect at the surface. The maximum temperature used for phase changes as well as the maximum liquid water content that can freeze is based on the Gibbs free-energy method. The snowpack is represented by a multilayer snow scheme of intermediate complexity. It simulates all the macroscopic physical properties of the snowpack in 12 layers, such as absorption of solar energy, heat content, compaction and density, snowmelt, water percolation, and water refreezing. Note that ISBA has been intensively validated with success against snow and ALT data in Siberian regions (Decharme et al., 2016, 2019). In the present study, ISBA uses, as meteorological forcing, data downscaled at 1 km resolution from the ERA-Interim reanalysis of the European Centre for Medium-Range Weather Forecast (Berrisford et al., 2011). Land hydrological and thermodynamical outputs from ISBA are given at daily intervals over the entire 2013 year on a 1 km resolution grid. To compute model initial conditions and ensure an adequate numerical equilibrium for soil water, ice and temperature, a spin-up of 50 years was performed with the ERA-Interim forcing by cycling the model over the 1979 to 1983 period before running it up to 2013.

3. Results

3.1. Process identification inside the freeze-thaw cycle

In the previous section, we adapted D-InSAR to forested areas by exploiting the polarimetric capability of the current SAR sensors. We demonstrated that polarimetric optimization of the coherence allows to estimate the ground movements under the forest because of the full temporal decorrelation of the canopy contribution between two successive acquisitions. As polarimetric optimization also maximizes the interferogram quality, the whole freeze-thaw cycle can be scanned with the highest possible temporal resolution, corresponding to the 11 day satellite revisit.

The deep winter, defined by daily averaged temperatures lower than −15 °C, during the period where the ground surface remains the most stable. The associated seven successive deformation maps are dominated by green color (Fig. 5a), revealing an almost null ground deformation at large scale (small scale colored patterns correspond to ice fracturing over lakes). Thermal inertia could delay the freeze of water in the ground at increasing depths, especially at the beginning of this period, but no deformation is perceptible. After winter, subsurface processes inducing deformation are identified and sorted in chronological order in Fig. 5b, along with the daily averaged atmospheric temperatures. The transition occurs as of early April, where the first positive temperatures cause Kolyma road deterioration because of melting (dark line on optimal coherence strip of Fig. 5a) and mark the end of the winter ground stability.

Spring season coincides with Lena break up, triggered by the upstream snow melt and ice pressure in conjunction with milder weather. Snow melt and ice jams cause inundation of the Lena River floodplain which results in a raise of the water level of more than 10 m, corresponding approximately to the half bank height (Fig. 6a). The blue squares on the graph of water level, recorded by the Yakutsk hydrographic station, are associated with the interferometric acquisitions, separated by 11 days. It appears that the deformation map integrates pressure on the river bank induced by almost the whole flood event. The deformation follows a decreasing gradient starting from the bank toward the highest terraces, which are also affected by subsidence because of ice melting. It is not accounted for an atmospheric effect, as it is confined under a strip close to the bank. Swelling occurring at the river boundary could be explained by infiltration of the flood waters in the aquifers of the cliff, facilitated because of accelerated thaw of the ground directly in contact with liquid water. In the circular zoom of Fig. 6a, white arrows indicate noisy interferometric phase forming linear features corresponding to surface waterways, always uncorrelated in differential interferograms. They are aligned along the global topographic gradient but situated on the most insolated south hillsides (open water appears first where there is the most insolation). A typical deformation pattern in summer (similar pattern is seen another time) can be found in Fig. 6b. It is characterized by anisotropic features perpendicular to the riverfront, oriented along the slope. The white arrows show that the deformation uplifts are associated with DEM depressions. In the circular zoom, white dashed lines show that deformation follows the shallow valleys that connect lakes and alaces, suggesting subsurface runoff.

3.2. Imaging the active layer thickness

Freezeback is a short transient period between a warm season, dominated by water movements, and a deep winter period, characterized by apparent stability of the ground (Fig. 5b). Deformation maps show ephemeral small-scale patterns from the middle of October, which persist over one month and a half (Fig. 7a). From December, these deformation patterns start to attenuate and almost reach the winter signature. The associated three time spans during which the deformation is integrated are symbolized by the widths of the cyan,

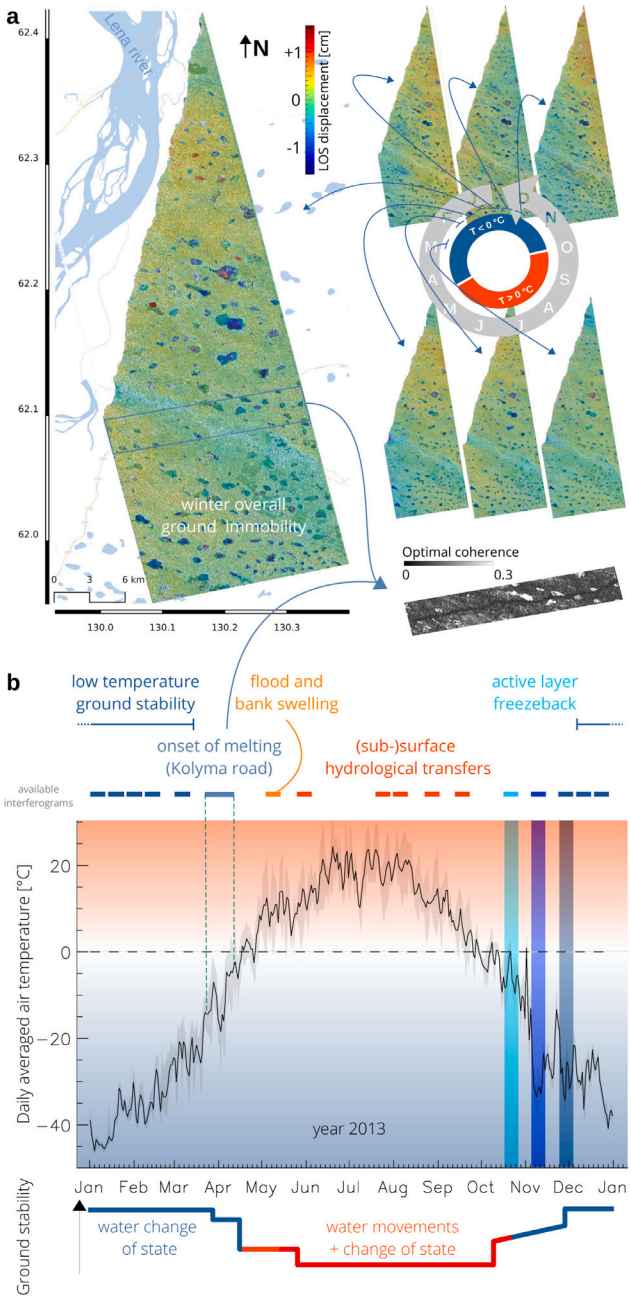

Fig. 5. Summary of the (sub-)surface processes occurring in the freeze-thaw cycle. a, Deformation maps, superimposed as alpha channel to a SAR intensity image, associated with the deep winter period. **b,** Chronological order of the identified (sub-)surface processes juxtaposed to the daily averaged air temperature (black) with its maximum spatial fluctuations on the data (grey). (For interpretation of the references to color in this figure legend, the reader is referred to the web version of this article.)

purple and grey lines in Figs. 5b and 7bc. Simulation of the ALT trend by ISBA model (Decharme et al., 2016, 2019) exhibits the maximum rate of ALT variation during this period, after the temperatures drop below zero degrees (Fig. 7b). The freeze front descends from the ground surface. The liquid water content which, at the beginning of freezeback, is already minimal in the upper part of the active layer continues to decrease in the lower part (Fig. 7c). ISBA simulations of soil layers associated with the most contrasted textures found in the region of Yakutsk (in clay-sand fraction terms) show a vertical offset in Fig. 7c because of different soil moistures, but synchronous behaviors. For both of these textures, end of October (cyan) corresponds to the most important variation of liquid and frozen soil water contents in the layer between 7 cm and 1.25 m, which comes down between 15 cm to 1.75 m in early November (purple), to a lesser extent. When reaching December (grey), the water state variations substantially attenuate over the whole depth range. In accordance with these simulations, the histogram of global deformation over the study area tends to become narrower and centered on zero when going from the first (cyan) to the third (grey) temporal interval (Fig. 7d). The ground deformation occurs in absence of hydrological transfers as the top group layer is frozen and the negative air temperature prevents from any rain percolation. During this period, the deformation can then be accounted for water state changes only which, over time, happens deeper in the ground and over a narrower vertical extent.

Considering described specifics, we inferred that these interferometric patterns were linked to the ALT and performed subsequent ground measurements using mechanical probing, in August 2020 when, according to ISBA simulations, the thawed depth corresponds to 89% of the ALT (the maximum thawed depth). The values are compensated of 11% even if this compensation is similar to the accuracy of the *in situ* measurement, as the values of roughness of the ground included in an interferometric phase averaging window is of order of 10 cm. From the 25 excavations, 4 were rejected because of close location to important interferometric phase transition zones, regarding the GPS localization accuracy (Supp material Fig. 2). It can be noted that ALT can vary from year to year because of different atmospheric forcing, but its spatial distribution remains stable as it depends on the ground properties. Fig. 8a clearly shows that the interferometric phase dynamics observed during freezeback is governed by ALT spatial distribution. The first two deformation integration periods (cyan and purple) exhibit very similar ground movement dynamics, in the whole ALT range, which considerably decreases when reaching winter (grey). Throughout these three stages, the maximum rate of water state variation occurs at increasing depths, though, with less amplitude. Within the whole freeze-thaw cycle, end of October-early November uniquely combines absence of rain with coupled surface runoff, on the one hand, and water state variation below the frozen surface over the widest possible vertical extent of the active layer, on the other hand. The induced ground movements reveal, hence, an image of the ALT spatial distribution. Note however that even if frost heaving dominates, subsidence is noticed for grounds of low ALT, that are predominantly more clayey and damp. In fact, clayay soils have higher field capacity, which is the water remaining in a soil after it has been thoroughly saturated and allowed to drain freely, usually for one to two days (Saxton et al., 1986; Pachepsky et al., 2001). They fill with more water than sandy soils during the heavy rainfall occurring before freezeback (Zakharova et al., 2018). The noticed subsidence suggests then lateral unfrozen water expulsion caused by freeze induced pressure (McRoberts and Morgenstern, 1975), toward -later frozen- deeper and more porous sand-dominated soils.

To clearly display the spatial pattern of the ALT repartition, two classes are defined on both sides of 1.40 m, corresponding to the transition from subsidence to heaving (Fig. 8b). At the regional scale, the ALT distribution shows a significant spatial anisotropy, which was discernable at local scale in the zoom of Fig. 7a. The orientation of deformation features follows relief meso-scale (DEM low frequency component), although less marked for the latter. At local scale, it is known that forest species influence the soil composition, and have an effect on the ALT (Fedorov et al., 2019). It appears that the correlation between ALT and NDVI is only partial. In that respect, the vegetation type cannot be used as an indicator of ALT.

The potential of Sentinel-1, providing global coverage and continuous survey, for imaging ALT is evaluated by forming interferograms during freezeback period of the year 2018. The assumption of total decorrelation of the vegetation component is done as X- and C-bands are close and the Sentinel-1 data are processed following the steps described above. Fig. 9 shows comparison of the obtained interferogram

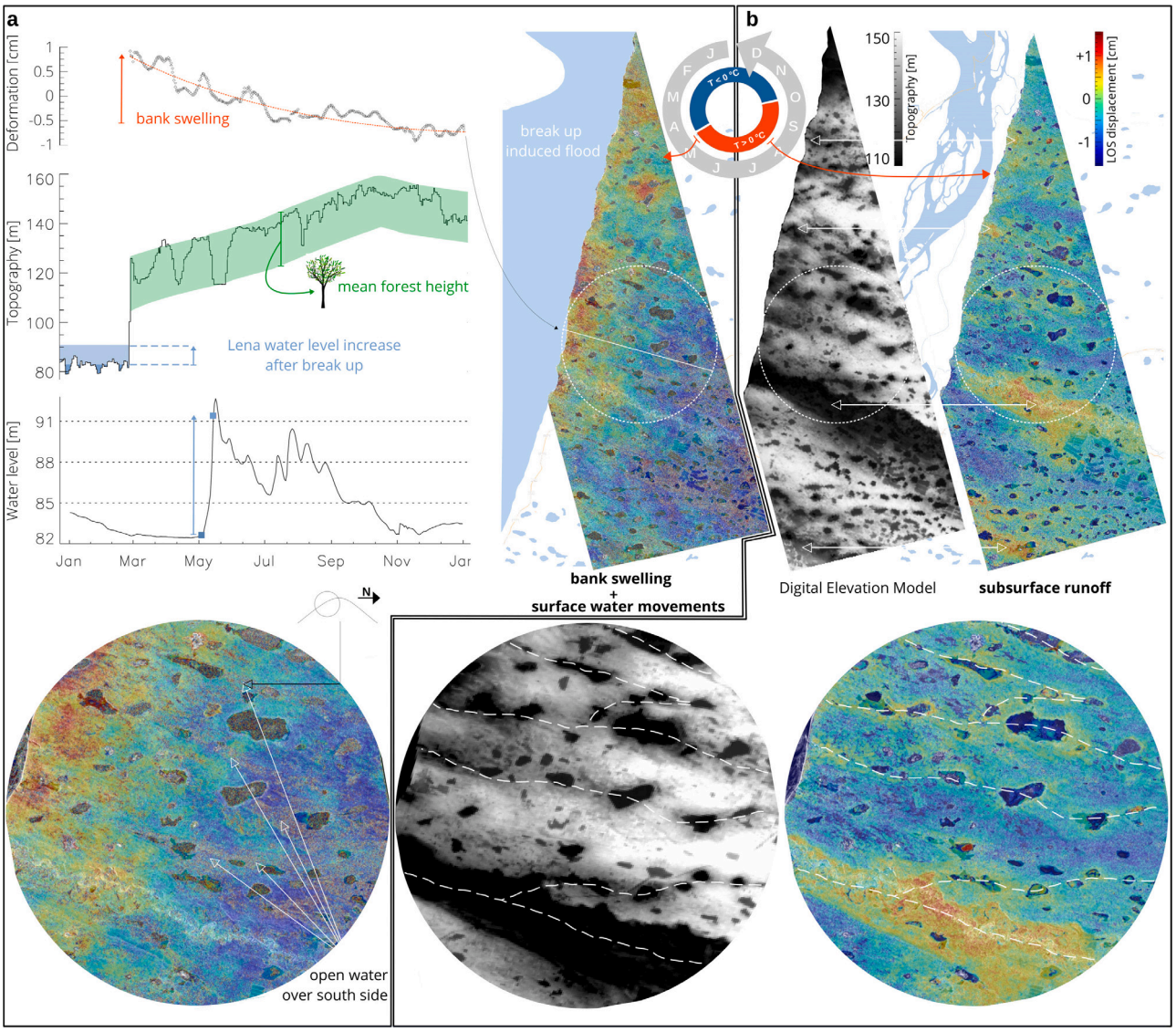

Fig. 6. Hydrological processes impact ground deformation during summer. a, Early May deformation map associated with ice break-up induced swelling with a circular zoom (right). Deformation profile, corresponding topographic profile and 2013 Yakutsk station hydrograph of the Lena River (left). As the topographic profile is extracted from ArcticDEM mosaic, estimated by non penetrative optical photogrammetry, the green strip symbolized the mean forest layer, of which the mean height has been assessed by ground measurements during summer 2012. **b,** Digital Elevation Model from ArcticDEM and deformation map of end of August revealing subsurface runoff. The white dashed lines indicate the identified runoff pathways.

with the previously presented TerraSAR-X's one. To maximize their similarities, Sentinel-1 interferogram, which has a coarser resolution, is not multilooked and both are represented over a specific color range. The interferometric phase patterns related to ALT distribution clearly appear with Sentinel-1, at a sufficiently high resolution to accurately map the ALT heterogeneity. It opens up new perspectives for ALT time monitoring at global scale as well as for improvement its accuracy from its temporal behavior.

These results allow us to put into perspective large-scale climate simulations that attempt to model and quantify the future evolution of soil carbon and associated carbon emissions to the atmosphere over periglacial regions. Soil Organic Carbon levels result from the interactions of several ecosystem processes, of which plant mortality, decomposition, and soil respiration are key. For a given Soil Organic Matter amount, these processes are partly determined by climatic factors, most importantly soil temperature and moisture. All these processes are currently simulated by climate models (Séférian et al., 2019). Using atmospheric forcing derived by the ERA-Interim reanalysis (Berrisford et al., 2011), the ISBA model tends to overestimate ALT. The bias reaches 60% compared to the mean InSAR derived ALT. This ALT overestimation also reveals a too warm soil temperature profile simulated by ISBA. Extrapolating these weaknesses to climate simulations and considering an uniform soil carbon vertical distribution (Fig. 8c), it also corresponds to the maximum bias of mobilizable carbon amount, i.e. the unfrozen soil carbon that can be lixiviated from the soil to rivers or released into the atmosphere as methane and carbon dioxide. Therefore, for given temperature and soil moisture conditions, this fact highlights that climate models could overestimate greenhouse gas emissions up to 60% over forested regions, but lower for non-uniform vertical distributions of the soil carbon. This results point out the need to have regionalized data-sets of ALT at the scale of boreal regions to benchmark and improve climate models.

4. Conclusions

Although permafrost is among the largest carbon reservoirs and is vulnerable to the present warming conditions, it remains poorly explored in reason of its wide extent and difficult access. Up to now, ALT

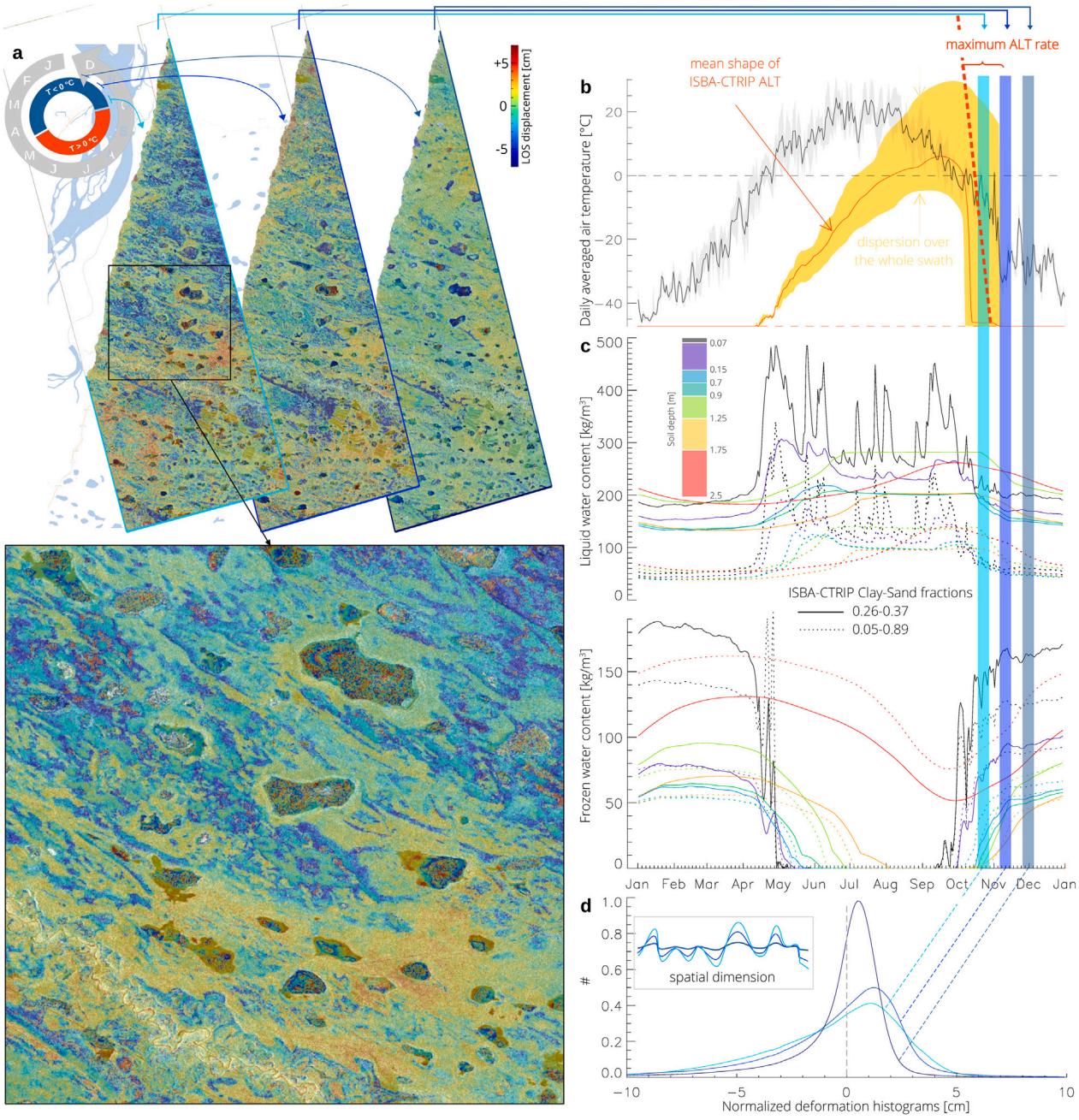

Fig. 7. Ground deformation during freezeback. a, Deformation integrated during three 11 day periods ranging from end of October until early December. **b,** Simulation of temperature and ALT shape by ISBA corresponding to the year of the data acquisition (2013). **c,** Temporal variations of liquid (top) and frozen (bottom) water contents at different soil layers (water contents have been integrated from 7 to 15 cm for the sake of clarity). The depth ranges are symbolized by different colors. Continuous and dotted lines correspond to the most contrasted textures (in clay-sand fraction terms) found in the region of Yakutsk. **d,** Deformation histograms associated with the three dates over the whole image. Qualitative spatial deformation profiles illustrate the ground behavior at the three dates in the box. (For interpretation of the references to color in this figure legend, the reader is referred to the web version of this article.)

is only sparsely sampled by probing techniques that are unable to assess its spatial heterogeneity. We demonstrated that SAR technique becomes the most relevant geophysical technique for permafrost survey. Indeed, aside from the wide coverage at high resolution, the short revisit of the all weather SAR sensors provides high enough temporal resolution to isolate ALT signature and the polarimetric capability allows to avoid the masking effect of the ubiquitous forest cover.

Based on ground measurements, it is demonstrated that the deformation occurring at freezeback is an indicator of ALT spatial distribution. In our approach, Land surface model first identifies the period of highest rate of thawed depth, occurring during freezeback. In fact, it has been shown that several processes happened within the freeze-thaw cycle and that the ratio between the thermodynamical and the hydrological components were the highest at this time. Therefore, ground movement estimation can be done independently over forest and bare grounds using polarimetric optimization to image the ALT distribution.

During freezeback, there is no liquid water on the ground (some liquid water only remains at the center of some freezing lakes), and the observed complex small scale patterns cannot be accounted for atmospheric effect, topographic residuals (height of ambiguity exceeds 200 m) or any other artifact. It cannot be accounted for calibration bias which is moreover constant over the whole image. Land surface

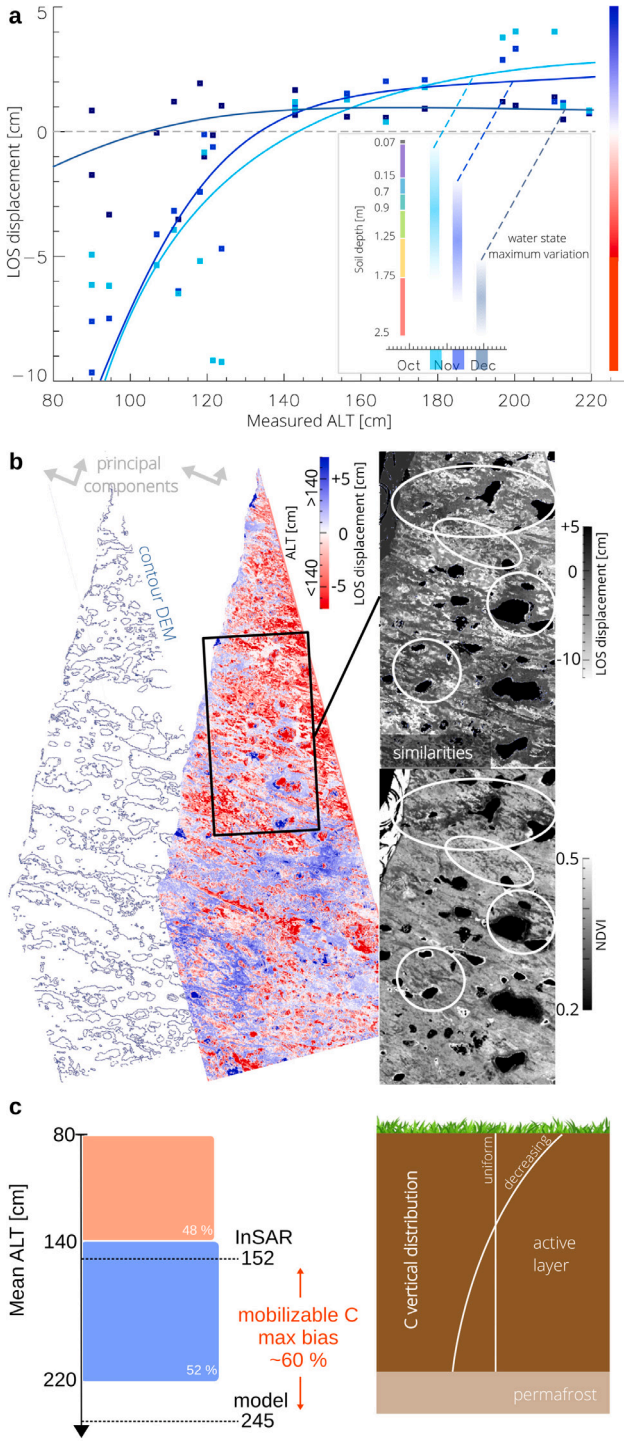

Fig. 8. Extraction of Active Layer Thickness from the deformation occurring during freezeback. a, Line Of Sight displacement as a function of ALT for the three 11 day periods ranging from end of October until early December (symbolized by the widths of the cyan, purple and grey lines in Figs. 5b and 7bc). In the box, the associated maximum water state variation in the soil is qualitatively symbolized by shadings. **b,** From left to right, DEM contour with 5 levels ranging from 80 to 160 m, two classes ALT map derived from LOS displacement (red: heaving, blue: subsidence, assumption of negligible horizontal movement is done because of absence of significant relief) and zooms of ALT map and NDVI (the grey scale is reversed for the latter to maximize the similarity). **c,** Comparison between InSAR derived statistical distribution of ALT, allocated in two classes, and ISBA model one (with a 18 cm standard deviation), obtained using geophysical forcing (left). 60% corresponds to the maximum bias of mobilizable Carbon amount in the case of a uniform vertical Carbon distribution (right).

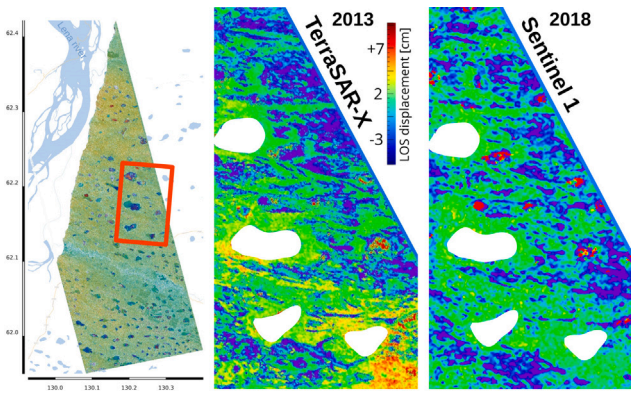

Fig. 9. Sentinel-1 potential for imaging ALT. Comparison of TerraSAR-X and Sentinel-1 interferograms, the latter is associated with the freezeback period of the year 2018.

modeling identifiates highest rate of the thawed depth at this time and accurate ground measurements unambiguously show correlation with ALT. Moreover, the next two successive independent interferograms show first similar but little attenuated patterns (for the first), and then almost "deep winter" null deformation (for the second), which is also in accordance with ISBA modeling. These patterns have a physical origin because we retrieved them with Sentinel-1 another year. These patterns are neither induced by vegetation: they are the continuous over the forest-clearing transitions of constant ALT.

It first emerged that ALT has a small-scale heterogeneity following continuous anisotropic patterns of main direction aligned along the main topographic gradient and, secondly, that ALT is only partially linked to the forest types. The complexity of the ALT spatial distribution results in the feedback between long-term hydrological history, vegetation and soil development and cannot be assessed using *in situ* measurements at large scale.

The approach we developed constitutes thus a new way for ALT time monitoring over the entire periglacial environment using the existing and future high resolution polarimetric SAR sensors emitting at high frequency (currently TerraSAR-X, Sentinel 1). Note that the imaged small scale spatial heterogeneity offers the possibility of permafrost dynamics monitoring with improved accuracy. ALT imaging could considerably ameliorate climate modeling, and especially the question about the future of greenhouse gas emissions in the light of climate change. Outside of the extreme northern regions, the effect of the higher biodiversity of the forested areas on the soils makes the models difficult to accurately estimate ALT and then green house gas emissions as highlighted before. Observing ALT spatial heterogeneities at regional scale is then all the more required. Conversely, it can enable consideration of lateral transfers at high resolution (Nelson et al., 1999; Beer et al., 2013; Fisher et al., 2018). It will also benefit to (sub-)surface hydrology, biogeochemistry, ecology, geomorphology and natural hazard management of the periglacial environment, which are strongly dependent on ALT (Bonnaventure and Lamoureux, 2013; Kokelj and Burn, 2005; Tashiro et al., 2020; Fedorov et al., 2019). It finally constitutes a new tool for the monitoring of global warming accelerated effects at the high latitudes.

The main challenge of global survey will concern the amount of data/information, which could be managed using the emerging AI techniques. Even if it is expected to be rare, atmospheric effects could affect the whole freezeback period and bias the interferometric phase over a given region. This would constitute a limitation for permafrost time monitoring, but not for ALT imaging because acquisitions could be done another year. Based on the knowledge of attenuation of the movement amplitude and on Land Surface Modelling, the advanced signal

processing techniques could nevertheless be employed to reconstruct the deformation patterns.

CRediT authorship contribution statement

F. Garestier: Conceptualization, Methodology, Validation, Formal analysis, Writing – original draft, Writing – review & editing, Visualization. **S. Guillaso:** Methodology, Validation, Formal analysis, Writing – original draft, Writing – review & editing. **E.A. Zakharova:** Methodology, Validation, Formal analysis, Writing – original draft, Writing – review & editing. **A.V. Kouraev:** Methodology, Validation, Formal analysis, Writing – original draft, Writing – review & editing. **B. Decharme:** Methodology, Validation, Formal analysis. **R.V. Desyatkin:** Methodology, Validation, Formal analysis. **A. Desyatkin:** Methodology, Validation, Formal analysis. **T. Chevalier:** Methodology, Validation, Formal analysis.

Declaration of competing interest

The authors declare that they have no known competing financial interests or personal relationships that could have appeared to influence the work reported in this paper.

Data availability

Data will be made available on request.

Acknowledgments

The authors would like to thanks CNES, France (TOSCA "PERMASENSING"), PNTS, France "PERMAFROST" and ANR, France "CLASSIQUE" for their financial support. We also thanks L. Perez and the DSI of Unicaen for their assistance. Finally, we thanks C. Delire for her helpful advices.

Appendix A. Supplementary data

Supplementary material related to this article can be found online at https://doi.org/10.1016/j.jag.2023.103582.

References

Abe, T., Iwahana, G., Efremov, P., Desyatkin, A., Kawamura, T., Fedorov, A., Zhegusov, Y., Yanagiya, K., Tadono, T., 2020. Surface displacement revealed by L-band InSAR analysis in the Mayya area, Central Yakutia, underlain by continuous permafrost. Earth Planets Space 72.

Antonova, S., Sudhaus, H., Strozzi, T., Zwieback, S., Kääb, A., Heim, B., Langer, M., Bornemann, N., Boike, J., 2018. Thaw subsidence of a Yedoma Landscape in Northern Siberia, measured in situ and estimated from TerraSAR-X Interferometry. Remote Sens. 10 (494).

Bartsch, A., Leibman, M., Strozzi, T., Khomutov, A., Widhalm, B., Babkina, E., Mullanurov, D., Ermokhina, K., Kroisleitner, C., Bergstedt, H., 2019. Seasonal progression of ground displacement identified with satellite radar interferometry and the impact of unusually warm conditions on permafrost at the Yamal Peninsula in 2016. Remote Sens. 11 (1865).

Beer, C., Fedorov, A., Torgovkin, Y., 2013. Permafrost temperature and active-layer thickness of Yakutia with 0.5-degree spatial resolution for model evaluation. Earth Syst. Sci. Data 5, 305–310.

Berardino, P., Fornaro, G., Lanari, R., Sansosti, E., 2002. A new algorithm for surface deformation monitoring based on small baseline differential SAR interferograms. IEEE Trans. Geosci. Remote Sens. 40, 2375–2383.

Berrisford, P., Dee, D.P., Poli, P., Brugge, R., Fielding, M., Fuentes, M., Kållberg, P.W., Kobayashi, S., Uppala, S., Simmons, A., 2011. The ERA-interim archive version 2.0 ERA report series. Shinfield Park. Reading.

Biggs, J., Wright, T., 2020. How satellite InSAR has grown from opportunistic science to routine monitoring over the last decade. Nature Commun. 11 (3863).

Biskaborn, B., Smith, S., Noetzli, J., Matthes, H., Vieira, G., Streletskiy, D., Schoeneich, P., Romanovsky, V., Lewkowicz, A., Abramov, A., Allard, M., Boike, J., Cable, W., Christiansen, H., Delaloye, R., Diekmann, B., Drozdov, D., Etzelmüller, B., Grosse, G., Guglielmin, M., Ingeman-Nielsen, T., Isaksen, K., Ishikawa, M., Johansson, M., Johannsson, H., Joo, A., Kaverin, D., Kholodov, A., Konstantinov, P., Kröger, T., Lambiel, C., Lanckman, J., Luo, D., Malkova, G., Meiklejohn, I., Moskalenko, N., Oliva, M., Phillips, M., Ramos, M., Sannel, A., Sergeev, D., Seybold, C., Skryabin, P., Vasiliev, A., Wu, Q., Yoshikawa, K., Zheleznyak, M., Lantuit, H., 2019. Permafrost is warming at a global scale. Nature Commun. 10.

Bombrun, L., Gay, M., Trouve, E., Vasile, G., Mars, J., 2009. DEM error retrieval by analyzing time series of differential interferograms. IEEE Geosci. Remote Sens. Lett. 6, 830–834.

Bonnaventure, P., Lamoureux, S., 2013. The active layer: A conceptual review of monitoring, modelling techniques and changes in a warming climate. Prog. Phys. Geogr. Earth Environ. 37, 352–376.

Breit, H., Fritz, T., Balss, U., Lachaise, M., Niedermeier, A., Vonavka, M., 2010. TerraSAR-X SAR processing and PRoducts. TGRS 48 (2).

Cavalié, O., Doin, M., Lasserre, C., Briole, P., 2007. Ground motion measurement in the Lake Mead area, Nevada, by differential synthetic aperture radar interferometry time series analysis: Probing the lithosphere rheological structure. J. Geophys. Res. 112.

Chen, J., Wu, Y., O'Connor, M., Cardenas, M.B., Schaefer, K., Michaelides, R., Kling, G., 2020. Active layer freeze-thaw and water storage dynamics in permafrost environments inferred from InSAR. Remote Sens. Environ. (ISSN: 0034-4257) 248, 112007. http://dx.doi.org/10.1016/j.rse.2020.112007.

Cloude, S., 2009. Polarisation: Applications in Remote Sensing. Oxford University Press, p. 10.

Cloude, S., Papathanassiou, K., 1998. Polarimetric SAR interferometry. IEEE Trans. Geosci. Remote Sens. 36, 1551–1565.

Cloude, S., Papathanassiou, K., 2003. Three-stage inversion process for polarimetric SAR interferometry. IEE Proc. Radar Sonar Navig. 150 (125).

Daout, S., Doin, M., Peltzer, G., Socquet, A., Lasserre, C., 2017. Large-scale InSAR monitoring of permafrost freeze-thaw cycles on the Tibetan Plateau. Geophys. Res. Lett. 44, 901–909.

De Zan, F., Krieger, G., Lopez-Dekker, P., 2013. On some spectral properties of TanDEM-X interferograms Over Forested Areas. IEEE Geosci. Remote Sens. Lett. 10, 71–75.

Decharme, B., Brun, E., Boone, A., Delire, C., Moigne, P., Morin, S., 2016. Impacts of snow and organic soils parameterization on northern eurasian soil temperature profiles simulated by the ISBA land surface model. Cryosphere 10, 853–877.

Decharme, B., Delire, C., Minvielle, M., Colin, J., Vergnes, J., Alias, A., Saint-Martin, D., Séférian, R., Sénési, S., Voldoire, A., 2019. Recent changes in the ISBA-CTRIP land surface system for use in the CNRM-CM6 climate model and in global off-line hydrological applications. J. Adv. Modelling Earth Syst. 11 (5).

Doin, M.-P., Guillaso, S., Jolivet, R., Lasserre, C., Lodge, F., Ducret, G., Grandin, R., 2011. Presentation of the small baseline NSBAS processing chain on a case example: The Etna deformation monitoring from 2003 to 2010 using Envisat data. In: Proceedings of FRINGE 2011. Frascati, Italy.

Fagan, J., Nelson, F., 2016. Spatial sampling design in the circumpolar active layer monitoring programme. Permafr. Periglac. Process 28, 42–51.

Fedorov, A., Konstantinov, P., Vasilyev, N., Shestakova, A., 2019. The influence of boreal forest dynamics on the current state of permafrost in Central Yakutia. Polar Sci. 22.

Fisher, J., Hayes, D., Schwalm, C., Huntzinger, D., Stofferahn, E., Schaefer, K., Luo, Y., Wullschleger, S., Goetz, S., Miller, C., Griffith, P., Chadburn, S., Chatterjee, A., Ciais, P., Douglas, T., Genet, H., Ito, A., Neigh, C., Poulter, B., Rogers, B., Sonnentag, O., Tian, H., Wang, W., Xue, Y., Yang, Z., Zeng, N., Zhang, Z., 2018. Missing pieces to modeling the Arctic-Boreal puzzle. Environ. Res. Lett. 13.

Flynn, T., Tabb, M., Carande, R., 2002. Coherence region shape extraction for vegetation parameter estimation in polarimetric SAR interferometry. In: IEEE International Geoscience and Remote Sensing Symposium. Toronto, Canada.

Fritz, T., Breit, H., Eineder, M., 2008. TerraSAR-X Products - Tips and Tricks. TerraSAR-X Science Meeting. 26/11/22008.

Garestier, F., Dubois-Fernandez, P., Papathanassiou, K., 2008. Pine forest height inversion using single-pass X-Band PolInSAR data. IEEE Trans. Geosci. Remote Sens. 46, 59–68.

Garestier, F., Toan, T., 2010a. Estimation of the backscatter vertical profile of a pine forest using single baseline P-band (Pol-)InSAR data. IEEE Trans. Geosci. Remote Sens. 48, 3340–3348.

Garestier, F., Toan, T., 2010b. Forest modeling for height inversion using single-baseline InSAR/Pol-InSAR data. IEEE Trans. Geosci. Remote Sens. 48, 1528–1539.

Goldstein, R., Werner, C., 1998. Radar interferogram filtering for geophysical applications. Geophys. Res. Lett. 25, 4035–4038.

Hosseini, S., Garestier, F., 2021. Pol-InSAR sensitivity to hemi-boreal forest structure at L- and P-bands. Int. J. Appl. Earth Obs. Geoinf. 94 (102213).

Kokelj, S., Burn, C., 2005. Geochemistry of the active layer and near-surface permafrost, Mackenzie delta region, Northwest Territories, Canada. Can. J. Earth Sci. 42, 37–48.

Lee, J., Pottier, E., 2017. Polarimetric Radar Imaging. CRC Press, p. 12.

Liu, L., Schaefer, K., Zhang, T., Wahr, J., 2012. Estimating 1992–2000 average active layer thickness on the Alaskan North Slope from remotely sensed surface subsidence. J. Geophys. Res. Earth Surf. 117.

Liu, L., Zhang, T., Wahr, J., 2010. Insar measurements of surface deformation over permafrost on the North Slope of Alaska. J. Geophys. Res. 115.

McRoberts, E., Morgenstern, N., 1975. Pore water expulsion during freezing. Can. Geotech. J. 12, 130–141.

Mishra, U., Hugelius, G., Shelef, E., Yang, Y., Strauss, J., Lupachev, A., Harden, J., Jastrow, J., Ping, C., Riley, W., Schuur, E., Matamala, R., Siewert, M., Nave, L., Koven, C., Fuchs, M., Palmtag, J., Kuhry, P., Treat, C., Zubrzycki, S., Hoffman, F., Elberling, B., Camill, P., Veremeeva, A., Orr, A., 2021. Spatial heterogeneity and environmental predictors of permafrost region soil organic carbon stockenvironss. Sci. Adv. 7 (9).

Morel, X., Decharme, B., Delire, C., Krinner, M., Hansen, B.U., Mastepanov, M., 2019. A new process-based soil methane scheme: Evaluation over arctic field sites with the ISBA land surface model. J. Adv. Modelling Earth Syst. 11 (1), 293–326.

Nelson, F., Shiklomanov, N., Mueller, G., 1999. Variability of active-layer thickness at multiple spatial scales, North-central Alaska, U.S.A.. Arctic Antarctic Alpine Res. 31, 179–186.

Pachepsky, Y.A., Timlin, D.J., Rawls, W.J., 2001. Soil water retention as related to topographic variables. SSoil Sci. Soc. Am. J. 65, 1787–1795.

Rouyet, L., Lauknes, T., Christiansen, H., Strand, S., Larsen, Y., 2019. Seasonal dynamics of a permafrost landscape, Adventdalen, Svalbard, investigated by insar. Remote Sens. Environ. 231 (111236).

Rouyet, L., Liu, L., Strand, S., Christiansen, H., Lauknes, T., Larsen, Y., 2021. Seasonal InSAR displacements documenting the active layer freeze and thaw progression in Central-Western Spitsbergen, Svalbard. Remote Sens. 13 (2977).

Saxton, K.E., Rawls, W.J., Romberger, J.S., Papendick, R.I., 1986. Estimating generalized soil–water characteristics from texture. Soil Sci. Am. J. 50, 1031–1036.

Schaefer, K., Liu, L., Parsekian, A., Jafarov, E., Chen, A., Zhang, T., Gusmeroli, A., Panda, S., Zebker, H., Schaefer, T., 2015. Remotely sensed active layer thickness (ReSALT) at Barrow, Alaska using interferometric synthetic aperture radar. Remote Sens. 7, 3735–3759.

Schuur, E., McGuire, A., Schädel, C., Grosse, G., Harden, J., Hayes, D., Hugelius, G., Koven, C., Kuhry, P., Lawrence, D., Natali, S., Olefeldt, D., Romanovsky, V., Schaefer, K., Turetsky, M., Treat, C., Vonk, J., 2015. Climate change and the permafrost carbon feedback. Nature 520, 171–179.

Séférian, R., Nabat, P., Michou, M., Saint-Martin, D., Voldoire, A., Colin, J., et al., 2019. Evaluation of CNRM Earth-System model, CNRM-ESM2-1: role of Earth system processes in present-day and future climate. J. Adv. Modelling Earth Syst. 11 (12), 4182–4227.

Shiklomanov, N., Streletskiy, D., Little, J., Nelson, F., 2013. Isotropic thaw subsidence in undisturbed permafrost landscapes. Geophys. Res. Lett. 40, 6356–6361.

Sica, F., Bretzke, S., Pulella, A., Bueso-Bello, J., Martone, M., Prats-Iraola, P., Gonzalez-Bonilla, M., Schmitt, M., Rizzoli, P., 2021. Insar decorrelation at X-Band from the joint TanDEM-X/PAZ constellation. IEEE Geosci. Remote Sens. Lett. 18, 2107–2111.

Strozzi, T., Antonova, S., Günther, F., Mätzler, E., Vieira, G., Wegmüller, U., Westermann, S., Bartsch, A., 2018. Sentinel-1 SAR interferometry for surface deformation monitoring in low-land permafrost areas. Remote Sens. 10 (1360).

Tashiro, Y., Yoh, M., Shiraiwa, T., Onishi, T., Shesterkin, V., Kim, V., 2020. Seasonal variations of dissolved iron concentration in active layer and rivers in permafrost areas. Russian Far East. Water 12 (2579).

Treuhaft, R., Gonzalves, F., Santos, J., Keller, M., Palace, M., Madsen, S., Sullivan, F., Graca, P., 2015. Tropical-forest biomass estimation at X-Band from the spaceborne TanDEM-X interferometer. IEEE Geosci. Remote Sens. Lett. 12, 239–243.

Voldoire, A., Saint-Martin, D., Sénési, S., Decharme, B., Alias, A., Chevallier, M., et al., 2019. Evaluation of CMIP6 DECK experiments with CNRM-CM6-1. J. Adv. Modelling Earth Syst. (11), 2177–2213.

Zakharova, E., Kouraev, A., Guillaso, S., Garestier, F., Desyatkin, R., Desyatkin, A., 2018. Recent dynamics of hydro-ecosystems in thermokarst depressions in Central Siberia from satellite and in situ observations: Importance for agriculture and human life. Sci. Total Environ. 615, 1290–1304.

Zimov, S., 2006. Climate change: Permafrost and the global carbon budget. Science 312, 1612–1613.

Zwieback, S., Meyer, F., 2021. Top-of-permafrost ground ice indicated by remotely sensed late-season subsidence. Cryosphere 15, 2041–2055.